2014

Quantumness and Coherence in Photosynthesis

Brian Doolittle
Colby College

Quantumness and Coherence in Photosynthesis

Brian Doolittle

May 20, 2014

Department of Physics and Astronomy
Colby College

Abstract

Long-lived oscillations lasting up to 1800 fs have been observed in the Fenna–Mathews–Olsen (FMO) Pigment-Protein complex. It is unclear if the oscillations are quantum or classical in origin. Quantized intra-pigment normal modes are responsible for these long-lived oscillations. In this thesis we simulate a bacteriachlorophyll dimer in the FMO Complex at physiological conditions. Our model describes two electronically coupled pigments coupled to the vibrational protein environment. Our goal is to find system parameters that allow long-lived quantum coherences to exist in photosynthetic complexes. We calculate the time evolution of our system's density matrix using the numerically exact quantum adiabatic path integral (QUAPI). The coherence of the system was determined by taking the real component of the density matrices complex off-diagonals. The quantumness of the system was determined by taking the Hilbert-Schmidt distance between the density matrix and its corresponding pointer states. By varying the Huang-Rhys factor, the reorganization energy difference, and the site energy difference we found long-lived coherences with an amplitude of 0.15 and a quantumness of 0.23. The quantum coherence was still present 2500 fs after the initial excitation of the system. This suggests that coherent quantum superpositions can theoretically occur in the FMO Complex at physiological conditions. The period of the coherent oscillations were on the same order of magnitude as the time resolution of our simulation causing aliasing to occur. In order to confirm the observed coherent superpositions we need to increase the temporal resolution of the simulation.

Acknowledgements

I would like to give my advisor Yoshi Sato many thanks for allowing me to be involved with his research and being a huge help to me along the way.

I would like to thank my parents and grandparent for supporting me at Colby.

I would like to thank the Colby Physics Department for giving me a great physics education and allowing us to use two of their computers full time.

Contents

1 Introduction

1.1 Purpose

The role of quantum mechanics in biological processes has interested physicist for a long time. Quantum effects may explain the near-unity efficiency exhibited by photosynthesis [1]. Recently, experimentalists have shown the existence of long-lived oscillatory behavior in Pigment-Protein Complexes (PPC's) such as the FMO protein [2]. The oscillations have been interpreted as a sign of electronic coherence. However, it is unclear if the observed oscillations are quantum or classical in origin [3]. The goal of this thesis is to determine if long-term quantum coherences can occur in photosynthetic complexes at physiological conditions.

Studying quantum effects in photosynthesis has useful applications in quantum computation. For a quantum algorithm to be implemented, there must be coherence among the quantum bits or qubits. However, environmental influences cause qubit systems to decohere quickly before any calculations can be made. Understanding how biology has managed to create long-term coherence can help us design better environments for qubits to live in [4, 5].

1.2 From Classical to Quantum

Before we discuss the nature and implications of quantum effects, we must first understand the meaning of classical. Anything that can be described by Newton's laws is considered classical. For example, if you run into a wall there *will* be an equal and opposite reaction (and a very unpleasant one at that). Newton's laws are the root of Fluid Dynamics, Electrodynamics, and Statistical Mechanics *i.e* anything we interact with on a daily basis can be described classically. Only when we go to the extremes of our universe does our trusty friend Newton begins to fail us–this is where things get interesting. Leaving our classical friend behind, let us delve into the realm of the extremely small, the extremely short-lived—the Quantum.

The quantum world is a strange one. Here, nothing has a defined position or velocity. Instead, quantum particles are described probabilistically as waves spreading out over space. For example, If you run into a wall in a quantum world, there *may* be an equal and opposite reaction, but then again, you might just end up on the other side of the wall. In fact, you wouldn't be existing on one side of the wall or the other, you'd be existing on both sides, simultaneously. This may seem very bizarre, but it comes from the fact that when we aren't looking at a quantum system, it is spread out over all of the possible states. It is only when we measure the system that it will collapse, with certain probability, into one of the classically possible states or the pointer states [6]. This probability is defined by the quantum system's wavefunction. Furthermore, the wavefunctions of different systems can overlap, much in the same way as classical waves. These overlaps or superpositons cause interferences leading to correlations between the two systems in ways that are not classically possible. The amount of correlation between the two wavefunctions is called the coherence. When the coherence is large, the two systems are said to be entangled. Measurement of one system entangled with another will cause the collapse of both wavefunctions into either correlated or anti-correlated states

[5, 7]. Quantum mechanics is not to be confused with statistical mechanics. While both theories are probabilistic in nature, statistical mechanics is a *classical* theory. Statistical mechanics is used to describe large ensembles of classical particles that are oscillating randomly due to thermal energy. Quantum mechanics differs in that the wavefunctions of these particles interfere with each other causing non-classical correlations.

We usually consider a system as either quantum or classical, however, this assumption is not always true. There is no fine line dividing these two physical realms. In reality, there is a blurred region at the molecular level where both quantum and classical effects are present. At this interface, systems require both classical and quantum theories. Photosynthetic processes occur in this quantum-classical realm. While photosynthetic energy transfer is a quantum process, interactions with the vibrational protein environment are classical. In general, classical environmental interactions with a quantum system destroys the correlations between the wavefunctions. This is called dephasing or decoherence. As the coherent superpositions dissolve, the system begins to turn into a classical statistical system. However, not all vibrations are classical, strong quantized vibrational frequencies or normal modes can occur at similar frequencies to the coherence [8]. Instead of causing the system to decohere, normal modes may assist the coherence allowing for long-term quantum effects. Thus, the presence of normal modes in a quantum system can counteract the decoherence leading to the long-term coherence observed in the FMO Complex [9, 2].

1.3 Photosynthesis Overview

Photosynthesis is the conversion of solar energy into chemical energy. It is the main source of energy for many organisms such as plants, algae, and some kinds of bacteria. The process is extremely efficient, over 90% of the absorbed photons are successfully stored as chemical energy [10]. Photosynthesis occurs at the molecular level in specialized organelles called chloroplasts. Pigment-Protein Complexes (PPCs) absorb light and transfer its energy to the reaction center where ionization occurs. The energy released through ionization is used to make ATP, a cellular form of chemical energy. ATP provides the energy to synthesize carbohydrates from hydrogen and carbon dioxide molecules. Through the process of photosynthesis, solar energy is successfully stored in the covalent bonds of the synthesized carbohydrates [10, 11].

In this thesis we are only concerned with the energy transfer from the PPCs to the reaction center. The transfer occurs between pigments in large arrays of PPCs called antenna complexes. PPCs are organized in the antenna complex such that high energy (blue light) absorbing pigments are located on the peripheries and low energy (red light) absorbing pigments are located close to the reaction center. This creates an energy gradient or "funnel" directing excitations or excitons from the peripheries to the reaction center. The funnel speeds up energy transfer by preventing excitons from wandering around the antenna complex to find the reaction center [11].

1.4 Pigment-Protein Complexes

In order to understand the energy transfer dynamics of the antenna complex, we must first look at the structure of the PPCs responsible for the energy transfer. PPCs consist of a

protein environment with specific bonding sites to which pigments can attach. The protein environment or bath is a dynamic structure made up of thousands of molecules, each molecule is constantly vibrating due to thermal energy in the bath. The pigments attached to the protein are also dynamic structures oscillating at quantized vibrational frequencies or normal modes [8]. These normal modes cause the energy levels of the pigments to split. Womick proposes that quantized normal modes in the FMO can promote quick transitions between electronic states [9]. Thus, coherent energy transfer is assisted by quantized intra-pigment normal modes.

Excitations or excitons are transferred between pigments through dipole interactions. When a pigment absorbs a photon, an excited state is created causing the charge to reorganize. The reorganization of charge creates an electronic dipole [12]. Two interacting dipoles are said to be electronically coupled. The strength of the electronic coupling is dependent on the distance between the pigments and their relative orientation [10, 11]. If the coupling is strong between two pigments then their wavefunctions overlap allowing for coherences to arise. Nuclear motion in the protein bath is responsible for the decoherence of these quantum superpositions [9]. Furthermore, couplings between nuclear degrees of freedom and the electronic system allows for energy to dissipate into the protein bath. When an electron becomes excited, it gives the nucleus a little "kick." In order to restore equilibrium, the nucleus must shift to a new position. Doing so removes energy from the electronic system and adds it to the bath. As the excitation is passed from pigment to pigment, the energy of the excitation will slowly dissipate into the environment. The amount of energy lost per transition is called the reorganization energy [12].

One of the most heavily studied PPCs is the Fenna-Mathews-Olson (FMO) Complex. The FMO was discovered in 1962 and was the first PPC to have its structure determined [11]. Today, its structure has been resolved to 1.9 Angstroms using x-ray crystallography. The FMO is composed of three identical monomer subunits. Each monomer contains 8 identical bacteriochlorophyll pigments. The site energy of each pigment is determined by its protein surroundings. Rivera *et al.* have experimentally determined the site energy for of each of the bacteriochlorophylls. Because of its well known structure and small number of pigments, the FMO monomer is ideal for studying the dynamics of photosynthetic energy transfer [13].

1.5 From Quantum to Classical

It is argued that the efficient energy transfer in the antenna complex is a result of excitonic superpositions. While classical excitons transfers between pigments based on a random walk or "incoherent hopping" model, quantum excitons traverse the antenna complex in the form of a coherent energy wavepacket [14]. The energy gradient in the antenna complex allows for excitons to quickly be transferred from the peripheries of the antenna complex to the reaction center. As excitons transfer between pigments, couplings with the environment cause their energy to dissipate into the environment. As the excitons lose energy, they will "flow" down the energy gradient from higher to lower energy. If the energy landscape were smooth, classical models would be able to transfer energy just as efficiently as quantum models. However, the energy landscape is very rugged, it contains many potential wells and barriers [2]. Classically if an exciton ended up in one of these potential wells, it would get stuck because its energy would be lower than that of the

surrounding pigments. However, if a quantum exciton got stuck in a potential well, it would be able to tunnel its way out with a certain probability. While the energy gradient contributes to the efficiency of the Antenna Complex, imperfections in the landscape can trap classical excitons. Thus, the presence of quantum effects allows for more efficient energy transfer.

Although quantum models may be better at traversing the rugged energy landscape, there are benefits to a classical models. Let me pose the following question: If an exciton is delocalized, in a superposition of states around the antenna complex, how would the wavefunction know to collapse when the reaction center was reached? Panitchayangkoon provides a clever solution to this problem. Energy transfer may in fact require both quantum and classical behavior. The exciton could begin in a quantum superposition, effectively traversing the rugged energy landscape. As it moves its way towards the reaction center, environmental fluctuations will cause energy loss and decoherence. If the energy transfer time of the antenna complex and the decoherence time of the exciton are on the same order, then the exciton would collapse into a classical excited state when it reached the reaction center allowing for ionization to occur [2].

2 Model and Theory

Modeling exciton dynamics in a PPC has proven to be a very difficult task. Models based purely on electronic energy transfer fail to predict the observed long-term coherence. At cryogenic temperatures (77 K) the observed coherence lasted for over 1800 fs [2]. Purely electronic models predict coherences of only 500 fs at 77 K [1]. To improve the model, the vibrational protein environment must be taken into consideration. The model must include both electronic couplings with other pigments and vibrational coupling with the environment.

Modeling molecular systems with both electronic and environmental coupling can be simplified by approximating the effects of the coupling. If the environmental coupling dominates the electronic coupling, then the system can be described with a classical incoherent hopping model. In this case, the electronic coupling is approximated with perturbation theory. If the electronic coupling dominates the environmental coupling, then the system is approximated as Markovian. Unfortunately, the electronic and environmental coupling in photosynthetic complexes are on the same order. Therefore, approximations cannot be used, the vibrational and electronic couplings must be considered explicitly in the model [4].

The model used in out simulation is based on a two-state electronic coupling model considering only the ground and excited states $|g\rangle$ and $|e\rangle$ respectively. The nuclear degrees of freedom can be included by coupling the electronic states with the vibrational bath of the protein. The physical structure of the bath is described with the spectral density [14]. The intra-pigment vibrational normal-modes cause the ground and excited states energies to split. The normal-modes can be removed from the bath and treated vibronically. Our two state electronic model then becomes a four state vibronic model [14].

2.1 The Pigment-Protein Hamiltonian

A pigment-protein (PP) can be modeled using the Molecular Hamiltonian [12]

$$H_{\text{mol}} = \sum_{a,b} |\phi_a\rangle\langle\phi_b| \otimes [\delta_{ab}\, H_a + (1 - \delta_{ab})\Theta_{ab}] \tag{1}$$

Where ϕ_a and ϕ_b represent the electronic states of the molecular system, H_a represents the normal-mode Hamiltonian, and Θ_{ab} describes the non-adiabatic couplings. H_a and Θ_{ab} are operators in the basis of the nuclear coordinates. Θ_{ab} is needed if the potential energy curves of the electronic states ϕ_a and ϕ_b overlap or are close enough together such that small changes in the radial distance from the nucleus, R, may result in electronic transitions. In short, if $R \to R + \Delta R$ causes $|\phi_a\rangle \to |\phi_b\rangle$ then Θ_{ab} is needed. For our Hamiltonian, we are only considering transitions between the ground state and a single excited state, $|g\rangle$ and $|e\rangle$ respectively. The potential energy curves of these states do not overlap allowing us to make the Born-Oppenheimer approximation setting $\Theta_{ab} = 0$ [12]. Thus we are left with the following Hamiltonian.

$$H_{mol} = \sum_a |\phi_a\rangle\langle\phi_a| \otimes H_a \tag{2}$$

H_a describes the nuclear motion of the protein environment for a given electronic state a. As the electronic state changes, the equilibrium point of the normal mode oscillators shift. To account for the shifting, we can use the same normal mode coordinates and just shift the minimum of the potential energy. Thus we have,

$$H_a = U_a + \sum_\xi \frac{\hbar\omega_\xi}{4}\left[P_\xi^2 + (Q_\xi + 2g_a(\xi))^2\right] \tag{3}$$

Where U_a is the vertical shift in the potential energy and the horizontal shift is expressed as

$$-2g_a(\xi) = \sqrt{\frac{2\omega_\xi}{\hbar}}\, q_\xi^{(a)}. \tag{4}$$

P_ξ and Q_ξ are dimensionless coordinates used to describe the harmonic oscillators. These can be expressed in terms of the creation and annihilation operators, $C_\xi^\dagger$ and C_ξ respectively.

$$Q_\xi = C_\xi + C_\xi^\dagger \tag{5}$$

$$P_\xi = -i(C_\xi - C_\xi^\dagger) \tag{6}$$

Where $C_\xi^\dagger$ and C_ξ obey the boson commutation relation

$$[C_\xi, C_{\xi'}^\dagger] = \delta_{\xi\xi'} \tag{7}$$

We can rewrite the normal-mode hamiltonian by gathering all of the terms dependent on ξ, the normal mode frequency, in a new Hamiltonian $H_{a,\xi}$

$$H_a = U_a + \sum_\xi H_{a,\xi} \tag{8}$$

We can rewrite $H_{a,\xi}$ by introducing the Displacement Operator

$$D^\dagger(g_a(\xi)) = exp[g_a(\xi)(C_\xi - C_\xi^\dagger)] \tag{9}$$

Now we have a means to transform the eigenstates of the non-shifted reference oscillators, $|N_\xi\rangle$, into eignestates of the shifted oscillator corresponding to state a, $|N_\xi^{(a)}\rangle$

$$|N_\xi^{(a)}\rangle = D^\dagger(g_a(\xi))|N_\xi\rangle \tag{10}$$

It is possible for the potential energy curves of the shifted oscillator states to overlap. Overlaps allow for easier transitions between shifted oscillator states. Assuming $|\chi_{aM}\rangle$ and $|\chi_{bN}\rangle$ are two normal mode eigenstates corresponding to two different modes, N and

M, and two different electronic states, a and b, the amount of overlap can be measured by the Franck-Condon factors given by

$$\langle \chi_{aM} | \chi_{bN} \rangle = \langle M | D(g_a) D^\dagger(g_b) | N \rangle \tag{11}$$

Let $H_\xi = \frac{\hbar\omega_\xi}{4}(P_\xi^2 + Q_\xi^2)$. Then using the Displacement Operator, we can rewrite $H_{a,\xi}$ as

$$H_{a,\xi} \equiv D^\dagger(g_a(\xi)) H_\xi D(g_a(\xi)) \tag{12}$$

The eigen-energies of $H_{a,\xi}$ have the following form

$$H_{a,\xi} \left| N_\xi^{(a)} \right\rangle = \hbar\omega_\xi \left(N_\xi^{(a)} + \frac{1}{2} \right) \left| N_\xi^{(a)} \right\rangle \tag{13}$$

Now let us introduce the identity operator in the basis of the normal modes,

$$I \equiv \bigotimes_\xi^f I_\xi = I_0 \otimes I_1 \otimes I_2 \cdots I_f \tag{14}$$

Where

$$I_f = \sum_{N_\xi=0}^{\infty} |N_\xi\rangle\langle N_\xi| \tag{15}$$

Then a mathematically rigorous expression of H_a is

$$\begin{aligned} H_a = U_a^{(0)} I &+ H_{a,0} \otimes I_1 \otimes I_2 \otimes \cdots \otimes I_f \\ &+ I_0 \otimes H_{a,1} \otimes I_2 \otimes \cdots \otimes I_f \\ &+ I_0 \otimes I_1 \otimes H_{a,2} \otimes \cdots \otimes I_f \\ &+ \cdots \\ &+ I_0 \otimes I_1 \otimes I_2 \otimes \cdots \otimes H_{a,f} \end{aligned} \tag{16}$$

The eigenket of H_a can now be written as

$$\begin{aligned} |\chi_{aN}\rangle &= \bigotimes_{\xi=0}^f |N_\xi^{(a)}\rangle \\ &= |N_0^{(a)}\rangle |N_1^{(a)}\rangle |N_2^{(a)}\rangle \cdots |N_f^{(a)}\rangle \end{aligned} \tag{17}$$

And the eigen-energies of H_a can be written as

$$H_a |\chi_{aN}\rangle = \left[U_a^{(0)} + \sum_\xi \hbar\omega_\xi \left(N_\xi^{(a)} + \frac{1}{2} \right) \right] |\chi_{aN}\rangle \tag{18}$$

$$\equiv \mathcal{E}(\chi_a) |\chi_{aN}\rangle \tag{19}$$

Now we can define the eigenket of H_{mol} as $|\psi_{aN}\rangle = |\phi_a\rangle \otimes |\chi_{aN}\rangle$

$$\begin{aligned} H_{\mathrm{mol}} |\psi_{aN}\rangle &= \sum_b |\phi_b\rangle\langle\phi_b|\phi_a\rangle \otimes [H_b|\chi_{aN}\rangle] \\ &= \sum_b \delta_{ab}|\phi_b\rangle \otimes [H_b|\chi_{bN}\rangle] \\ &= |\phi_a\rangle \otimes [H_a|\chi_{aN}\rangle] \\ &= \mathcal{E}(\chi_a)|\psi_{aN}\rangle. \end{aligned} \tag{20}$$

Taking the inner product of our vibrational eigenkets, we find that

$$\langle\chi_{aM}|\chi_{bN}\rangle = \delta_{ab}\prod_{\xi=0}^{f}\delta_{M_\xi^{(a)}\,N_\xi^{(b)}} + (1-\delta_{ab})\prod_{\xi=0}^{f}\langle M_\xi^{(a)}|N_\xi^{(b)}\rangle. \tag{21}$$

Where $\chi_{aM} \equiv M_\xi^{(a)}$ and $\chi_{bN} \equiv N_\xi^{(b)}$. The first term on the right-hand side of the equality necessitates the orthonormaility of the eigen basis of each normal mode. The second term is just the Franck-Condon factors as defined earlier. In our pigment-protein model, we are only considering two states, ground and excited, $|g\rangle$ and $|e\rangle$ respectively. Thus, our molecular Hamiltonian becomes

$$H_{\mathrm{mol}} = |g\rangle\langle g| \otimes H_g^{(nm)} + |e\rangle\langle e| \otimes H_e^{(nm)} \tag{22}$$

If we take our reference set of normal mode oscillators to be that of the ground state, then the minimum of the ground state PES will be located at the origin. Thus, our normal modes need no shifting and $U_g^{(0)} = 0$ and $g_g(\xi) = 0$ giving us

$$H_g = \sum_\xi \frac{\hbar\omega_\xi}{4}\left[P_\xi^2 + Q_\xi^2\right] \tag{23}$$

Since there is no displacement of our oscillators, we do not need the Displacement Operator to define our eigenkets. Thus, the eigenkets of our ground state are just the eigenkets of the normal-mode oscillators

$$|N_\xi^{(g)}\rangle = |N_\xi\rangle \tag{24}$$

For the excited state Hamiltonian, H_e, we must include the shift of the reference set of oscillators, thus

$$H_e^{(nm)} = U_e^{(0)} + \sum_\xi \frac{\hbar\omega_\xi}{4}\left[P_\xi^2 + (Q_\xi + 2g_\xi)^2\right] \tag{25}$$

$$= \hbar\epsilon + H_g^{(nm)} + \sum_\xi \hbar\omega_\xi g_\xi Q_\xi \tag{26}$$

where a shorthand notation $g_\xi \equiv g_e(\xi)$ has been introduced. The site energy, $\hbar\epsilon$, is defined

$$\hbar\epsilon = U_e^{(0)} + \sum_\xi \hbar\omega_\xi g_\xi^2 \tag{27}$$

For an exciton isolated to a single pigment, we define the system basis to be that of the electronic states alone, $\{|g\rangle,|e\rangle\}$. We can then rewrite H_{mol} as the following

$$H_{\text{mol}} = H_S \otimes I_B + I_S \otimes H_B + S \otimes B \tag{28}$$

Where

$$H_S = \hbar\epsilon|e\rangle\langle e| \tag{29}$$
$$H_B = H_g \tag{30}$$
$$S = |e\rangle\langle e| \tag{31}$$
$$B = \sum_\xi^f \hbar\omega_\xi g_\xi Q_\xi \tag{32}$$
$$I_S = |g\rangle\langle g| + |e\rangle\langle e| \tag{33}$$
$$I_B = \bigotimes_{\xi=0}^f I_\xi \tag{34}$$

We can include the first normal mode, $\xi = 0$, explicitly into our System Hamiltonian, H_S, by defining a new orthonormal basis $\{|g\rangle|M_0\rangle, |e\rangle D_0^\dagger|N_0\rangle, \}$, where $D_0 = D(g_e(0)) = D(g_0)$ and $|N_0\rangle$ is an infinite set of vibrational eigenstates. The Displacement Operator is not needed for the vibrational eigenstates of the ground state because the ground state was defined so that the minimum of the PES was at the origin. We can now write the Hamiltonian in terms of the new electro-vibronic basis. While the form remains the same, $H_{\text{mol}} = H_S \otimes I_B + I_S \otimes H_B + S \otimes B$, each component is split so that

$$H_S = |g\rangle\langle g| \otimes H_0 + |e\rangle\langle e| \otimes (\hbar\epsilon I_0 + D_0^\dagger H_0 D_0), \tag{35}$$
$$H_B = \sum_{\xi=1}^f \frac{\hbar\omega_\xi}{4}\left(P_\xi^2 + Q_\xi^2\right) \tag{36}$$
$$S = |e\rangle\langle e| \otimes I_0 \tag{37}$$
$$B = \sum_{\xi=1}^f \hbar\omega_\xi g_\xi Q_\xi \tag{38}$$
$$I_S = (|g\rangle\langle g| + |e\rangle\langle e|) \otimes I_0, \tag{39}$$
$$I_B = \bigotimes_{\xi=1}^f I_\xi \text{ with } I_\xi = \sum_{N_\xi=0}^\infty |N_\xi\rangle\langle N_\xi|. \tag{40}$$

Here, I_0 is the the indentity operator belonging to $\xi = 0$

$$I_0 = \sum_{M_0=0}^{\infty} |M_0\rangle\langle M_0| = \sum_{N_0=0}^{\infty} D_0^\dagger |N_0\rangle\langle N_0| D_0 \tag{41}$$

and H_0 is the Hamiltonian of the non-shifted normal mode at $\xi = 0$

$$H_0 = \frac{\hbar\omega_0}{4}(P_0^2 + Q_0^2) \tag{42}$$

Since the first normal mode was excluded from the bath, we must rewrite the site energy summing from the $\xi = 1$ normal mode rather than the $\xi = 0$.

$$\hbar\epsilon = U_e + \sum_{\xi=1}^{f} \hbar\omega_\xi g_\xi^2 \tag{43}$$

To simplify our notation, we can substitute M_0 and N_0 with μ and ν respectively and make the following definitions

$$|g_\mu\rangle \equiv |g\rangle|M_0 = \mu\rangle \tag{44}$$
$$|e_\nu\rangle \equiv |e\rangle D_0^\dagger |N_0 = \nu\rangle \tag{45}$$

Furthermore, the eigenenergy of $D_0^\dagger|\nu\rangle$ is

$$E_\nu \equiv \hbar\omega_0 \left(\nu + \frac{1}{2}\right) \tag{46}$$

We can get some useful eigenvalue expressions using the orthonormality of the vibronic basis. *i.e* $\langle g_\mu|e_\nu\rangle = 0$ and $\langle g_\mu|g_\nu\rangle = \langle e_\mu|e_\nu\rangle = \delta_{\mu\nu}$

$$H_S\,|g_\mu\rangle = E_\mu\,|g_\mu\rangle \tag{47}$$
$$H_S\,|e_\nu\rangle = (\hbar\epsilon + E_\nu)\,|e_\nu\rangle \tag{48}$$
$$S\,|g_\mu\rangle = 0 \tag{49}$$
$$S\,|e_\nu\rangle = |e_\nu\rangle. \tag{50}$$

Using these eigenvalues, we can rewrite H_S, S, and I_S

$$H_S = \sum_{\mu=0}^{\infty} E_\mu |g_\mu\rangle\langle g_\mu| + \sum_{\nu=0}^{\infty} (\hbar\epsilon + E_\nu)|e_\nu\rangle\langle e_\nu| \tag{51}$$

$$S = \sum_{\nu=0}^{\infty} |e_\nu\rangle\langle e_\nu| \tag{52}$$

$$I_S = \sum_{\mu=0}^{\infty} (|g_\mu\rangle\langle g_\mu| + |e_\mu\rangle\langle e_\mu|) \tag{53}$$

Let us now define a new operator called the Excitation Operator

$$V_{eg} \equiv |g\rangle\langle e| \otimes I_0 = |g\rangle\langle e| \otimes \sum_{\sigma=0}^{\infty} |\sigma\rangle\langle\sigma| \tag{54}$$

The action on the vibronic exciton basis is

$$V_{ge}|g_\nu\rangle = 0 \tag{55}$$

$$V_{ge}|e_\nu\rangle = |g\rangle \sum_{\sigma=0}^{\infty} |\sigma\rangle\langle\sigma|D_0^\dagger|\nu\rangle = \sum_{\sigma=0}^{\infty} |g_\sigma\rangle (FC)_{\sigma\nu} \tag{56}$$

$$V_{eg}|g_\nu\rangle = |e\rangle|\nu\rangle \tag{57}$$

$$V_{eg}|e_\nu\rangle = 0 \tag{58}$$

where $(FC)_{\sigma\nu}$ is a Franck-Condon factor for a special case of $a = g$ and $b = e$, that is $(FC)_{\sigma\nu} \equiv \langle\chi_{g\sigma}|\chi_{e\nu}\rangle$. The matrix elements of this operator are obtained as $\langle g_\mu|V_{ge}|e_\nu\rangle = (FC)_{\mu\nu}$ and $\langle g_\mu|V_{ge}|g_\nu\rangle = \langle e_\mu|V_{ge}|e_\nu\rangle = \langle e_\mu|V_{eg}|g_\nu\rangle = 0$ due to the orthogonality among the electronic states, $\langle g|e\rangle = 0$. Likewise for an operator defined as V_{eg} we get $\langle e_\mu|V_{eg}|g_\nu\rangle = \langle g_\nu|V_{ge}|e_\mu\rangle^* = \langle\chi_{g\nu}|\chi_{e\mu}\rangle = (FC)_{\nu\mu}$, and other elements vanish. (Note that the Fracnk-Condon factors are all real.) Using $\Delta g_{ge} = g_g(0) - g_e(0) = -g_0$, the explicit form of Franck-Condon factor is obtained from Eq.(2.105) as

$$(FC)_{\mu\nu} = e^{-g_0^2/2} \sum_{m=0}^{\mu} \sum_{n=0}^{\nu} \frac{(-1)^m g_0^{m+n}}{m!n!} \sqrt{\frac{\mu!\nu!}{(\mu-m)!(\nu-n)!}} \delta_{\mu-m,\nu-n} \tag{59}$$

The symmetry under interchange of indeces is $(FC)_{\mu\nu} = (-1)^{\nu-\mu}(FC)_{\nu\mu}$ for $\nu > \mu$. Here, the Huang-Rhys factor S_{HR} is defined as $g_0 = -\sqrt{S_{HR}}$ [12]. The Huang-Rhys factor describes the amount of overlap between the vibrational modes. This leads to

$$(FC)_{0\nu} = e^{-g_0^2/2} \frac{g_0^\nu}{\sqrt{\nu!}} = e^{-S_{\mathrm{HR}}/2} \frac{(-1)^\nu S_{\mathrm{HR}}^{\nu/2}}{\sqrt{\nu!}}. \tag{60}$$

in which $(FC)_{\nu 0} = (-1)^\nu (FC)_{0\nu}$ holds.

2.2 Pigment-Protein Dimer

It is easy to expand the Pigment-Protein Monomer to the Dimer (PPD). The Hamiltonian simply takes the form of

$$H = H_{\mathrm{mol},1} \otimes I_{\mathrm{mol},2} + I_{\mathrm{mol},1} \otimes H_{\mathrm{mol},2} + V_{\mathrm{ex}} \tag{61}$$

Where $H_{\mathrm{mol},m}$ is just the Molecular Hamiltonian for Pigment-Protien Monomer with m as the site index

$$H_{\mathrm{mol},m} = H_{Sm} \otimes I_{Bm} + I_{Sm} \otimes H_{Bm} + S_m \otimes B_m \tag{62}$$

$$I_{\mathrm{mol},m} = I_{Sm} \otimes I_{Bm} \tag{63}$$

V_{ex} is the inter-monomer excitonic coupling that is insensitive about the baths,

$$V_{\text{ex}} = V_{12} \otimes I_{B2} \tag{64}$$

We let the excitonic coupling operator to be

$$V_{12} = \hbar J_{12} \left(V_{eg} \otimes V_{ge} + V_{ge} \otimes V_{eg} \right) \tag{65}$$

Separating the Dimer Hamiltonian into the independent System and Bath operators, the Hamiltonian can be rewritten in the form $H = H_S \otimes I_B + I_S \otimes H_B + H_{SB}$ where

$$H_S = H_{S1} \otimes I_{S2} + I_{S1} \otimes H_{S2} + V_{12} \equiv \sum_{m=1}^{2} H_{Sm} + \sum_{m<n}^{2} V_{mn} \tag{66}$$

$$H_B = H_{B1} \otimes I_{B2} + I_{B1} \otimes H_{B2} \equiv \sum_{m=1}^{2} H_{Bm} \tag{67}$$

$$H_{SB} = S_1 \otimes I_{S2} \otimes B_1 \otimes I_{B2} + I_{S1} \otimes S_2 \otimes I_{B1} \otimes B_2 \equiv \sum_{m=1}^{2} S_m \otimes B_m \tag{68}$$

$$I_S = I_{S1} \otimes I_{S2} \tag{69}$$

$$I_B = I_{B1} \otimes I_{B2} \tag{70}$$

In the vibronic exciton basis, we have $\{|g_\mu\rangle|g_\nu\rangle\}$ for zero-exciton manifold, $\{|e_\mu\rangle|g_\nu\rangle, |g_\mu\rangle|e_\nu\rangle\}$ for one-excition manifold, and $\{|e_\mu\rangle|e_\nu\rangle\}$ for two-exciton manifold. For our model we will only be considering the one-exciton manifold and we can define our basis as

$$|1, \mu\nu\rangle \equiv |e_\mu\rangle|g_\nu\rangle \tag{71}$$

$$|2, \mu\nu\rangle \equiv |e_\mu\rangle|g_\nu\rangle \tag{72}$$

The actions of operators onto these basis are obtained as

$$H_{S1}|1, \mu\nu\rangle = (\hbar\epsilon_1 + E_\mu)|1, \mu\nu\rangle \tag{73}$$

$$H_{S2}|1, \mu\nu\rangle = E_\nu|1, \mu\nu\rangle \tag{74}$$

$$V_{12}|1, \mu\nu\rangle = \hbar J_{12} \sum_{\sigma=0}^{\infty} (FC)_{\sigma\mu}|g_\sigma\rangle(|e\rangle|\nu\rangle) \tag{75}$$

$$H_{S2}|2, \mu\nu\rangle = (\hbar\epsilon_2 + E_\nu)|1, \mu\nu\rangle \tag{76}$$

$$H_{S1}|2, \mu\nu\rangle = E_\mu|1, \mu\nu\rangle \tag{77}$$

$$V_{12}|2, \mu\nu\rangle = \hbar J_{12}(|e\rangle|\mu\rangle) \sum_{\sigma=0}^{\infty} (FC)_{\sigma\nu}|g_\sigma\rangle \tag{78}$$

which lead to

$$\langle 1, \mu'\nu'|V_{12}|1, \mu\nu\rangle = 0 \tag{79}$$

$$\langle 2, \mu'\nu'|V_{12}|1, \mu\nu\rangle = \hbar J_{12}(FC)_{\mu'\mu}(FC)_{\nu\nu'} \tag{80}$$

$$\langle 1, \mu'\nu'|V_{12}|2, \mu\nu\rangle = \hbar J_{12}(FC)_{\mu\mu'}(FC)_{\nu'\nu} \tag{81}$$

$$\langle 2, \mu'\nu'|V_{12}|2, \mu\nu\rangle = 0 \tag{82}$$

so that the matrix element of the system's Hamiltonian is obtained as

$$\langle 1,\mu'\nu'|H_S\,|1,\mu\nu\rangle = (\hbar\epsilon_1 + E_\mu + E_\nu)\delta_{\mu'\mu}\delta_{\nu'\nu} \tag{83}$$
$$\langle 2,\mu'\nu'|H_S\,|1,\mu\nu\rangle = \hbar J_{12}(FC)_{\mu'\mu}(FC)_{\nu\nu'} \tag{84}$$
$$\langle 1,\mu'\nu'|H_S\,|2,\mu\nu\rangle = \hbar J_{12}(FC)_{\mu\mu'}(FC)_{\nu'\nu} \tag{85}$$
$$\langle 2,\mu'\nu'|H_S\,|2,\mu\nu\rangle = (\hbar\epsilon_2 + E_\mu + E_\nu)\delta_{\mu'\mu}\delta_{\nu'\nu} \tag{86}$$

Likewise,

$$S_1|1,\mu\nu\rangle = |1,\mu\nu\rangle \tag{87}$$
$$S_1|2,\mu\nu\rangle = 0 \tag{88}$$
$$S_2|1,\mu\nu\rangle = 0 \tag{89}$$
$$S_2|2,\mu\nu\rangle = |2,\mu\nu\rangle \tag{90}$$

for arbitrary μ and ν values. These relations imply that

$$S_1 = \sum_{\mu=0}^{\infty}\sum_{\nu=0}^{\infty}|1,\mu\nu\rangle\langle 1,\mu\nu| \tag{91}$$
$$S_2 = \sum_{\mu=0}^{\infty}\sum_{\nu=0}^{\infty}|2,\mu\nu\rangle\langle 2,\mu\nu| \tag{92}$$

so that

$$H_{SB} = \sum_{m=1}^{2}\sum_{\mu=0}^{\infty}\sum_{\nu=0}^{\infty}|m,\mu\nu\rangle\langle m,\mu\nu|\otimes B_m \tag{93}$$

The final three pieces of our Hamiltonian can be written

$$\begin{aligned} H_S = &\sum_{m=1}^{2}\sum_{\mu,\nu=0}^{\infty}\hbar\left[\epsilon_m + (\mu+\nu)\omega_0\right]\,|m,\mu\nu\rangle\langle m,\mu\nu| \\ &+ \hbar J_{12}\sum_{\mu,\nu,\mu',\nu'=0}^{\infty}\left[(FC)_{\mu\mu'}(FC)_{\nu'\nu}|1,\mu'\nu'\rangle\langle 2,\mu\nu| + (FC)_{\mu'\mu}(FC)_{\nu\nu'}|2,\mu'\nu'\rangle\langle 1,\mu\nu|\right] \end{aligned} \tag{94}$$

$$H_B = \sum_{m=1}^{2}\sum_{\xi\neq 0}\hbar\omega_\xi C^\dagger_{\xi,m}C_{\xi,m}, \tag{95}$$

$$H_{SB} = \sum_{m=1}^{2}\sum_{\mu,\nu=0}^{\infty}|m,\mu\nu\rangle\langle m,\mu\nu|\sum_{\xi\neq 0}\hbar\omega_\xi g_{\xi,m}(C_{\xi,m} + C^\dagger_{\xi,m}). \tag{96}$$

H_S describes the intrinsic dynamics of an exciton in the two coupled pigments. Its eigenstates, $|E_\alpha\rangle$, are referred to as the vibronic eigenstates. The Hamiltonian H_B describes the vibrations in the surrounding protein bath. H_{SB} describes the coupling between a pigment and its bath. There are no direct couplings between baths. The physical structure of the

baths is described by the spectral density functions $G_m(\omega) = \hbar\omega^2 \sum_{\xi\neq 0} g^2_{\xi,m}\, \delta(\omega - \omega_\xi)$ for $m = 1, 2$. In our model we are using the B777 spectral density that can be approximated with

$$G_m(\omega) = \hbar\omega \left(\frac{\lambda_m}{\lambda_0}\right) \sum_{s=1}^{3} c_s \left(\frac{\omega}{\omega_{cs}}\right)^{s-1} e^{-\omega/\omega_{cs}}, \tag{97}$$

where $\lambda_0 = 107\,\mathrm{c}m^{-1}$, $c_1 = 0.22$, $c_2 = 0.78$, $c_3 = 0.31$, $\omega_{c1} = 170\,\mathrm{c}m^{-1}$, $\omega_{c2} = 34\,\mathrm{c}m^{-1}$, $\omega_{c3} = 69\,\mathrm{c}m^{-1}$, and the reorganization energy of Pigment-Protein monomer is defined as $\hbar\lambda_m = \int_0^\infty d\omega\, G_m(\omega)/\omega$.

2.3 The Reduced Density Operator

The quantum state of the vibronic exciton is described by the reduced density operator, $\rho(t)$, for the system, H_S. It can be obtained by tracing out the bath modes from the density operator, W, of the whole PPD system, H [12, 15]. That is

$$\rho(t) = \mathrm{T}r_{\xi\neq 0}\{W(t)\} \tag{98}$$

By tracing out the bath modes, we are condensing all of the bath's information into an 8-state vibronic system considering the normal mode splitting of the ground and excited states. This is done by taking an average of sorts over the influence of the bath modes on the vibronic system [5]. In our data analysis we will trace out the vibronic modes leaving the density matrix of a two state electronic system. However, this two-state system does not act like an electronic system, each component of the reduced density matrix is scaled by a vibronic factor.

2.4 Optical Excitation of System

For the PPD, the transition dipole operator is readily obtained as $\boldsymbol{D} = \boldsymbol{D}_1^{(PP)} + \boldsymbol{D}_2^{(PP)}$ with $\boldsymbol{D}_m^{(PP)}$ the transition dipole of mth PP. This operator describes absorption of a photon that induces a transition from a ground state of PPD into an one-exciton state of PPD as $\langle 1, \mu'\nu'|\boldsymbol{D}|g_\mu\rangle|g_\nu\rangle = \boldsymbol{d}_1\,(FC)_{\mu\mu'}\delta_{\nu\nu'}$ and $\langle 2, \mu'\nu'|\boldsymbol{D}|g_\mu\rangle|g_\nu\rangle = \boldsymbol{d}_2\,\delta_{\mu\mu'}(FC)_{\nu\nu'}$, where $\boldsymbol{d}_m$ is the transition dipole moments of mth pigment [12].

The transition dipole moment of vibronic-exciton state $|E_\alpha\rangle$ from various ground-electronic phonon states is thus obtained as

$$\boldsymbol{d}_\alpha^{(ex)} = \sum_{m=1}^{2} \sum_{\mu,\nu,\mu',\nu'=0}^{\infty} f_{\mu\nu}\langle E_\alpha|m, \mu'\nu'\rangle\langle m, \mu'\nu'|\boldsymbol{D}|g_\mu\rangle|g_\nu\rangle, \tag{99}$$

where $f_{\mu\nu}$ are the weight of ground states that satisfy $\sum_{\mu,\nu} |f_{\mu\nu}|^2 = 1$ to conserve the total oscillator strength of PPD. In thermal equilibrium, the weight is proportional to populations of the ground states so that $f_{\mu\nu} = \exp\{-(\mu+\nu)\hbar\omega_0/k_BT\}/\sum_{\nu'}\exp\{-2\hbar\omega_0\nu'/k_BT\}$, and this approaches $f_{\mu\nu} \simeq \delta_{\mu 0}\delta_{\nu 0}$ at the low temperature limit.

For an optical transition achieved by an ultrashort laser pulse, $\boldsymbol{E}(t) \propto \boldsymbol{e}\delta(t)$ with $\boldsymbol{e}$ the polarization vector, shot into a sample in which PPDs are randomly oriented in solvent, the reduced density matrix at $t = 0$ in the vibronic exciton base is obtained as [8]

$$\rho_{\alpha\beta}(0) \equiv \langle E_\alpha|\rho(0)|E_\beta\rangle = \frac{\boldsymbol{d}_\alpha^{(ex)} \cdot \boldsymbol{d}_\beta^{(ex)}}{\sum_{\alpha'} \boldsymbol{d}_{\alpha'}^{(ex)} \cdot \boldsymbol{d}_{\alpha'}^{(ex)}} \tag{100}$$

where the denominator is needed for normalization, $\mathrm{T}r\,\rho(0) = \sum_\alpha \rho_{\alpha\alpha}(0) = 1$.

2.5 Numerical Method

In order to obtain the non-perturbative and non-Markovian dynamics of the reduced density operator, we have employed the quasi-adiabatic propagator path integral method (QUAPI). This method was first developed by Makri and Makarov [16, 17], and then extended to handle exciton transfer under multiple baths by Nalbach et al [4, 18].

The system-bath basis of M Pigment-Proteins (PPs) can be taken as

$$|\boldsymbol{s}, \boldsymbol{b}\rangle = |s_1\rangle|s_2\rangle \cdots |s_M\rangle \otimes |b_1\rangle|b_2\rangle \cdots |b_M\rangle \tag{101}$$

Which works as

$$\begin{aligned} S_j \otimes B_j|\boldsymbol{s}, \boldsymbol{b}\rangle &= |s_1\rangle \cdots |s_{j-1}\rangle(S_j|s_j\rangle)|s_{j+1}\rangle \cdots |s_M\rangle \\ &\quad \otimes |b_1\rangle \cdots |b_{j-1}\rangle(B_j|b_j\rangle)|b_{j+1}\rangle \cdots |b_M\rangle && (102)\\ &= |\boldsymbol{s}\rangle \otimes |b_1\rangle \cdots |b_{j-1}\rangle(s_j B_j|b_j\rangle)|b_{j+1}\rangle \cdots |b_M\rangle && (103)\\ & && (104) \end{aligned}$$

Take $H_{env} = H_B + H_{SB}$, then the action of H_{env} on the system-bath basis is

$$\begin{aligned} H_{env}|\boldsymbol{s}, \boldsymbol{b}\rangle &= |\boldsymbol{s}\rangle \otimes \sum_{j=1}^{M} \left(H_{B_j} + s_j B_j + \hbar\mu_j s_j^2\right)|\boldsymbol{b}\rangle && (105)\\ &\equiv |\boldsymbol{s}\rangle \otimes H_{env}(\boldsymbol{s})|\boldsymbol{b}\rangle && (106) \end{aligned}$$

Here we write

$$H_{env}(\boldsymbol{s}) = \sum_{j=1}^{M} H_{env,j}(s_j) \tag{107}$$

Since $[H_{env,j}(s_j), H_{env,k}(s_k)] = 0$ holds for $j \neq k$, we have for compex z,

$$e^{zH_{env}(\boldsymbol{s})} = e^{zH_{env,1}(s_1)} \otimes \cdots e^{zH_{env,j}(s_j)} \otimes e^{zH_{env,M}(s_M)}, \tag{108}$$

Where the Baker-Campbell-Hausdorff relation has been used. Thus, the quasi-adiabatic propagator can be expressed as [19]

$$\begin{aligned} \langle \boldsymbol{s'}, \boldsymbol{b'}|e^{-iH\Delta t/\hbar}|\boldsymbol{s}, \boldsymbol{b}\rangle &= \langle \boldsymbol{s'}, \boldsymbol{b'}|e^{-iH_{env}\Delta t/2\hbar}e^{-iH_S\Delta t/\hbar}e^{iH_{env}\Delta t/2\hbar}|\boldsymbol{s}, \boldsymbol{b}\rangle + \mathcal{O}(\Delta t^3) && (109)\\ &= \langle \boldsymbol{s'}|e^{-iH_S\Delta t/\hbar}|\boldsymbol{s}\rangle\langle \boldsymbol{b'}|e^{-iH_{env}(\boldsymbol{s'})\Delta t/2\hbar}e^{iH_{env}(\boldsymbol{s})\Delta t/2\hbar}|\boldsymbol{b}\rangle + \mathcal{O}(\Delta t^3) && (110)\\ &= K_0(\boldsymbol{s}, \boldsymbol{s'}; \Delta t)\prod_{j=1}^{M}\langle b_j'|e^{-iH_{env,j}(s_j')\Delta t/2\hbar}e^{iH_{env,j}(s_j)\Delta t/2\hbar}|b_j\rangle + \mathcal{O}(\Delta t^3). && (111) \end{aligned}$$

Here $K_0(\boldsymbol{s}, \boldsymbol{s}'; \Delta t)$ describes the time evolution of the system and the product describes the time evolution of the bath. Because we've discretized time, the $\mathcal{O}(\Delta t^3)$ term to accounts for the error in our calculation. The error is based on our time step Δt. The influence of the bath on the system is given by the influence functional

$$I_{\mathrm{FV}}[\boldsymbol{s}^+, \boldsymbol{s}^-, t] = \prod_{j=1}^{M} I_{\mathrm{FV},j}[s_j^+, s_j^-; t] \tag{112}$$

$$= \prod_{j=1}^{M} \exp\left\{-\frac{1}{\hbar}\Phi_j[s_j^+, s_j^-; t]\right\} \tag{113}$$

$$= \exp\left\{-\frac{1}{\hbar}\sum_{j=1}^{M} \Phi_j[s_j^+, s_j^-; t]\right\} \tag{114}$$

Where $\boldsymbol{s}^+$ describes the forward time evolution of the system and $\boldsymbol{s}^-$ describes the backward time evolution. The influence phase due to the j-th bath is given by

$$\Phi_j[s_j^+, s_j^-; t] = \int_0^t dt' \, \left\{s_j^+(t') - s_j^-(t')\right\} \int_0^{t'} dt'' \, \left\{C_j(t'-t'')s_j^+(t'') - C_j^*(t'-t'')s_j^-(t'')\right\} \tag{115}$$

Where $C_j(t)$ is the bath correlation function of the j-th bath,

$$C_j(t) = \hbar \int_0^\infty d\omega \, G_j(\omega) \left[\coth\left(\frac{\hbar\omega}{2k_B T}\right)\cos\omega t - i\sin\omega t\right] \tag{116}$$

The QUAPI scheme can be discretized by replacing the integrals in the influence phase with sums.

$$\Phi_j[s_j^+, s_j^-; t] = \sum_{k=0}^{N}\sum_{k'=0}^{k} \left(s_{j,k}^+ - s_{j,k}^-\right)\left(C_{kk'}^{(j)} s_{j,k'}^+ - C_{kk'}^{(j)*} s_{j,k'}^-\right) \tag{117}$$

so that the total influence phase is obtained as

$$\Phi_{\mathrm{FV}}[\boldsymbol{s}^+, \boldsymbol{s}^-; t] = \sum_{j=1}^{M}\sum_{k=0}^{N}\sum_{k'=0}^{k} \left(s_{j,k}^+ - s_{j,k}^-\right)\left(C_{kk'}^{(j)} s_{j,k'}^+ - C_{kk'}^{(j)*} s_{j,k'}^-\right) \tag{118}$$

Giving us an Influence Functional of

$$I_{\mathrm{FV}}[\boldsymbol{s}^+, \boldsymbol{s}^-, t] = exp\left\{-\frac{1}{\hbar}\sum_{j=1}^{M}\sum_{k=0}^{N}\sum_{k'=0}^{k} \left(s_{j,k}^+ - s_{j,k}^-\right)\left(C_{kk'}^{(j)} s_{j,k'}^+ - C_{kk'}^{(j)*} s_{j,k'}^-\right)\right\} \tag{119}$$

Here, $s_{j,k} = s_j(k\Delta t)$, $s_{j,k'} = s_j(k'\Delta k_{max})$, and $C_{kk'}^{(j)} = C_j(k\Delta t - k'\Delta k_{max})$ where N is the number of time steps, k and k' are iteration parameters for the system and bath respectively, and Δt and Δk_{max} are the time increments of the system and bath respectively. The memory time of the system is given by $\Delta t \Delta k_{max}$.

While the math may seem intimidating, the concept is simple. The evolution of the density matrix is the sum of all possible paths traversing both forward and backward in time from the current state, $s_{j,k}$.The forward time evolution is given by $s^+(t)$, the sum of all paths connecting $s_{j,k}$ to $s_{j,N}$. The backward time evolution is given $s^-(t)$, the sum of all paths connecting $s_{j,k}$ to $s_{j,0}$.

The precision of the method is determined by the following two parameters: Δt, the time resolution and Δk_{max}, the degree of inclusion of non-Markovian memory effect of the relaxation dynamics of bath. QUAPI is non-perturbative, it does not consider the coupling between the system and the bath, but looks at the dynamics directly. If $\Delta t \to 0$ and $\Delta k_{max} \to 0$ then we can calculate the exact dynamics of the reduced density operator $\rho(t)$. Thus, QUAPI is said to be numerically exact. Since these limits are computationally unattainable, we must find accurate finite values for these parameters. The resolution Δt needs to be short enough to see temporal changes of population (and coherence). This is determined by the largest of J_{12} in our PPD model. Choosing a value of $\Delta t = 25$ fs should be small enough to see these temporal changes. The memory time $\Delta t \Delta k_{max}$ needs to be taken long enough to include the non-Markovian memory effects. These are determined by the bath correlation function (116). At large values of t, our spectral density (97) decreases rapidly. Choosing a memory time of 50 fs covers 80% of the real part of the decay and 50% of the imaginary part of the decay of the bath correlation function. With a memory time of 50 fs and time slice of 25 fs, we can deduce that $\Delta k_{max} = 2$ fs.

2.6 Quantumness

As an exciton is being continuously influenced by the thermal bath, its electronic coherence will decohere and therefore approach the most classical state that is often referred to as the pointer state [6]. In order to quantify how far the reduced density operator $\rho(t)$ is from the pointer state, we employ the quantumness $Q(\rho)$ proposed by Giraud *et al.* [7]

$$Q(\rho) = \mathrm{m}in||\rho - \rho_c|| \tag{120}$$

where ρ_c is a density operator of the classical state in consideration. Thus the quantumness of a given reduced density operator ρ is defined as the minimum of the Hilbert-Schmidt distance (denoted by $||A|| \equiv \sqrt{\mathrm{T}r(AA^\dagger)}$ for arbitrary operator A) measured from various classical states.

The the most classical state for the vibronic exciton PPD is its thermal equilibrium, the Boltzmann state for the bath temperature. We therefore take the pointer state as the diagonal of the vibronic exciton states, $\sum_\alpha c_\alpha |E_\alpha\rangle\langle E_\alpha|$ where c_α are real coefficients [6]. Hence the quantumness is

$$Q(t) \equiv \min_{\{c_\alpha\}} \left\| \rho(t) - \sum_\alpha c_\alpha |E_\alpha\rangle\langle E_\alpha| \right\| \tag{121}$$

where c_α are determined to minimize the Hilbert-Schmidt distance for $\rho(t)$. The has the bounds $0 \leq Q(t) \leq \sqrt{1 - 1/d}$, where d is the number of vibronic exciton states. Thus, in a two state system like we are considering, the maximum quantumness is ≈ 0.7.

3 Data and Analysis

3.1 The Simulation

Our simulation is based in Mathematica and models an electronically coupled Pigment-Protein dimer surrounded by a protein bath. Each pigment is coupled to its own localized bath. There is no coupling between the individual baths. The simulation was designed to be as general as possible. The following parameters can be adjusted:

- Normal Mode Frequency (ω_0)
- Huang-Rhys Factor (S)
- Electronic Coupling (J)
- Site Energy ($\hbar\epsilon$)
- Temperature (T)
- Reorganization Energy (λ)
- Dipole Orientation
- Length of Simulation
- Time Slice (Δt)
- Iteration Parameter (Δk_{max})

The simulation can have three different initial conditions. The first is a specific excited state represented in the site basis. The second is a specific excitation energy represented in the energy basis. The third is an excitation by an ultrashort laser pulse. Ultrashort laser pulses are quantum in nature initially exciting the dimer into a superposition. The Simulation constructs the Hamiltonian from the parameters then uses the QUAPI to calculate the time evolution of the density matrix. All of our data is retrieved from the density matrix as it evolves in time. For all of our calculations we set the number of intra-pigment normal modes in the ground and excited state to 1, considering only one vibrational energy splitting. For our QUAPI calculation, we set Δt to 25 fs, Δk_{max} to 2, and t to 2500 fs.

Testing our simulation, we found that at 125 k, purely electronic coherences lasted just over 500 fs and vibronic coherences to at least 2500 fs. These values correspond to length of coherence observed by Christensson *et al.* for electronic and vibronic models [1]. Thus, our simulation corresponds with literature results.

3.2 Data Collection

Our goal is to use the simulation to see if long-term quantum coherence can theoretically occur at physiological conditions in a PPD . We focused on changing three parameters, the Huang-Rhys factor (S), site energy difference ($\Delta\epsilon$), and reorganization energy difference

(a)

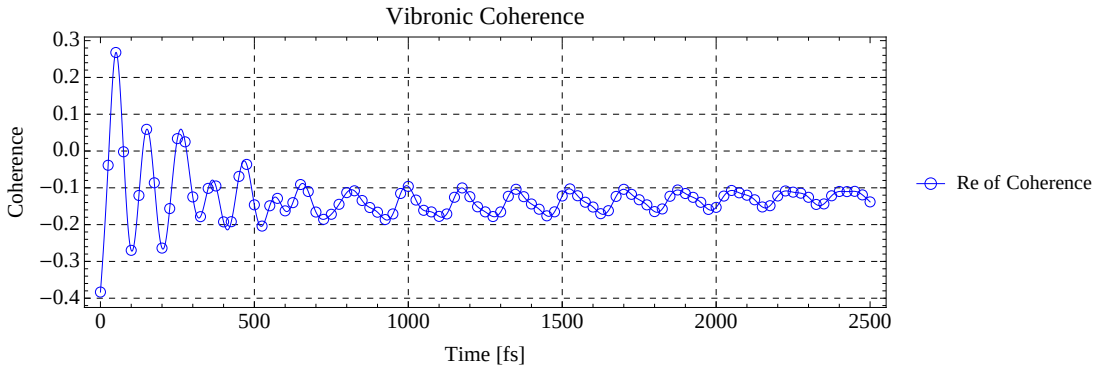

(b)

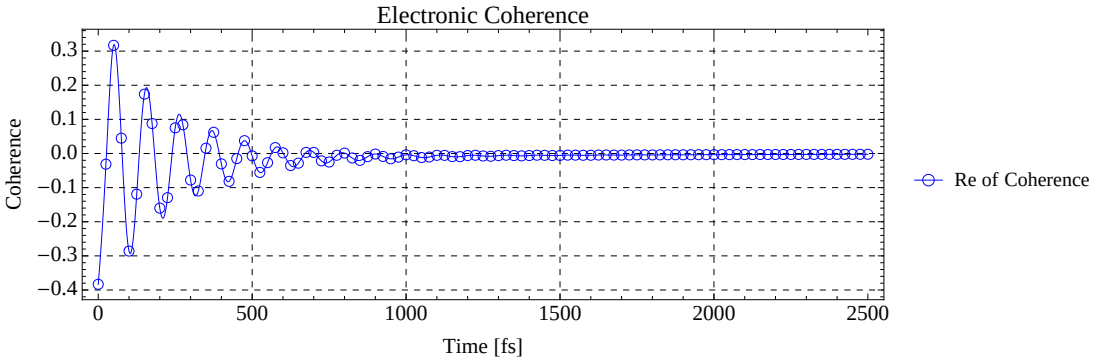

Figure 1: The plots show the coherence for a vibronic trial (top) and an electronic trial (bottom) for a temperature of 125 k.

($\Delta\lambda$). These parameters have been experimentally determined, $\Delta\epsilon$ ranges from 50 $\rightarrow$ 230 cm^{-1}, $\Delta\lambda$ ranges from 2 $\rightarrow$ 23 cm^{-1}, S is 0.02. The physiological values for the parameters we held constant are as follows the coupling (J) ranges from 32 $\rightarrow$ 98 cm^{-1}, the reorganization energy (λ) ranges from 11 $\rightarrow$ 38 cm^{-1}, and the temperature T was set to 300 k [20, 21].

We began our data collection by varying the Huang-Rhys factor with the site energy difference. Our normal mode frequency, ω_0, was set to 191 cm^{-1} as experimentally determined by Rätsep *et al.* To see the full effect of the Huang-Rhys factor, we varied it from 0.0 to 0.3. The physiological value of 0.0196 is included within this range.The site energy of Pigment-Protein 1 (PP1) was set to 13500 cm^{-1} and the site energy difference was varied from 0 $\rightarrow$ $2\omega_0$. We took data at a temperature 300 k, with a coupling of 100 cm^{-1}, and a reorganization energy of 15 cm^{-1} for each pigment.

Next, we varied the reorganization energy difference against the site energy difference. ω_0 was set to 191 cm$^{(}-1$), T was set to 300 k, J was set to 100 cm^{-1}, λ was set to 15 cm^{-1}, S was set to 0.02, and the site energy of PP1 was set to 13500 cm^{-1}. $\Delta\epsilon$ was varied from 0 $\rightarrow$ $2\omega_0$ cm^{-1}, and $\Delta\lambda$ was varied from $-5 \rightarrow 5$ cm^{-1}.

Our last data set modeled the orientation and coupling of BChl3 and BChl4 in the FMO dimer [21]. $\Delta\epsilon$ was varied from $-1.5\omega_0 \rightarrow 1.5\omega_0$ cm^{-1}, $\Delta\lambda$ was varied from $-15 \rightarrow -2$ cm^{-1}, and S was tested at the value of 0.02 and 0.2. J was set to 59 cm^{-1}, λ was set to 25 cm^{-1}, T was set to 300 k, and ω_0 was set to 180 cm^{-1}.

3.3 Data Analysis

Our data was interpreted from the reduced density matrix described by eq. 98. The main focus was to investigate long-lived quantumness and coherence in the FMO. Our quantitative measure of quantumness was defined in the theory section by eq. 121. Since we have a two state system, the maximum quantumness is $1/\sqrt{2} \approx 0.7$. At each time slice in the simulation the quantumness was calculated fig. 2.

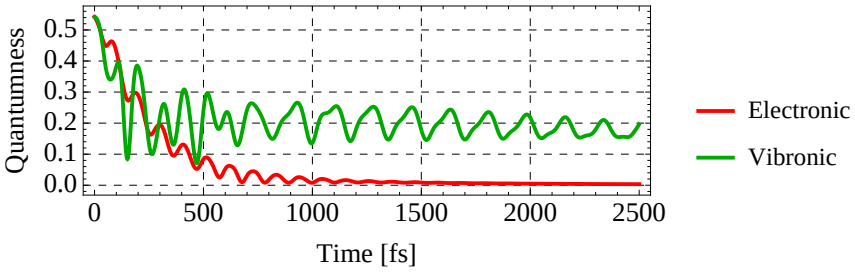

Figure 2: The graph shows the time evolution of the quantumness for 2500 fs after excitation. The vibronic case is in green and the electronic case is in red. The Huang-Rhys factor was set to 0.1.

There is initially a large amount of quantumness that is attributed to the electronic coherence (red). The electronic coherence quickly decays after a few hundred femtoseconds. The vibronic quantumness decreases initially with the electronic quantumness however, it reaches a minimum value around 500 fs and stabilizes there. This long-term quantumness is what we are interested in. To isolate the long-term quantum effects, we only considered the data in the time range of 1500 to 2500 fs. To quantify the long-term quantum effects, we took the average of the quantumness over the considered time range.

The Coherence measures the correlation or superposition of quantum states. Coherence is determined by the complex off diagonals of the density matrix fig. 3. The maximum amplitude that the coherence can have is 1.

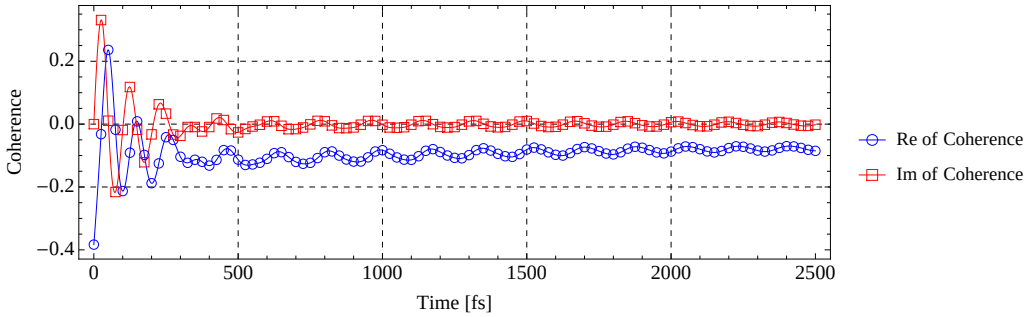

Figure 3: The graph shows the coherence of the exciton for 2500 fs after excitation. The red corresponds to the imaginary part of the coherence and the blue corresponds to the real part of coherence. The Huang-Rhys factor was set to 1.

The coherence has a large amplitude for the first 300 femtoseconds this is due to the electronic coherence. Afterwards, there are smaller amplitude oscillations that correspond to the long-lived coherence. To quantify the long-term coherence, took the root-mean-square (rms) of the amplitude from 1500 to 2500 fs.

4 Results and Discussion

4.1 General Trends

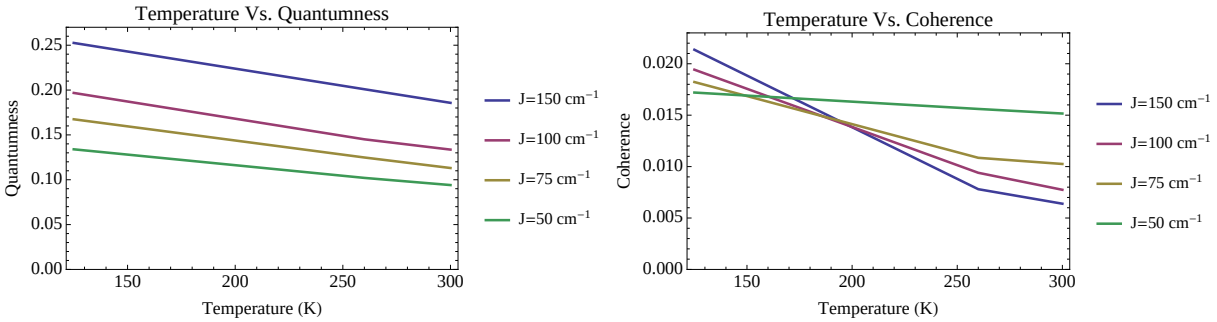

Figure 4: The graphs plot quantumness (left) and coherence (right) against temperature. Each data set has the same parameters except for for the electronic coupling. The electronic coupling, J, is in units of cm^{-1}.

As the temperature increases, the quantumness and coherence decrease, fig. 4. This is due to the temperature dependence in bath correlation function eq. 116. As the temperature increases, nuclear vibrational motion also increases causing quicker energy dissipation and decoherence. This trend is constant throughout our data sets. Furthermore, Temperature does not affect the features in the data, it only affect the amplitude of the features fig. 5.

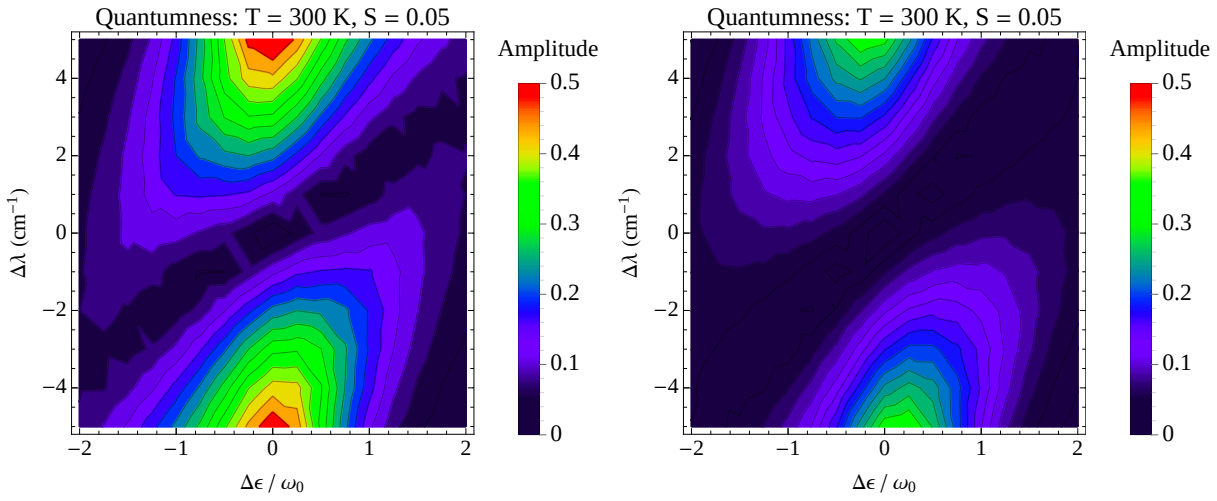

Figure 5: The contour plots show the quantumness for various reorganization energy differences, $\Delta\lambda$, and energy differences, $\Delta\epsilon/\omega_0$, in the FMO dimer. The data at 125 K is shown on the left and the data at 300 K is shown on the right. Both plots are scaled the same magnitude. Notice that the general shape of the peaks is the same.

4.2 The Huang-Rhys Factor

Quantumness is dependent on both the Huang-Rhys factor and the site energy difference fig. 6 (a). As S increases, the quantumness also increases. Since the Huang-Rhys factor is a measure of overlap between vibrational states, we would expect that higher values of S have more coherence. However, there is a certain value of S where the quantumness will saturate. Increasing S past this point will not increase the quantumness. The saturation point of the maximum in fig. 6 occurs at $S = 0.01$ for $\Delta\epsilon/\omega_0$ ranging from 1.5 to 2.0. The maximum quantumness in our data set is 0.1245. The coherence has a maximum of 0.0072 at a Huang-Rhys factor of 0.01 and a site energy difference of 1.5 fig. 6 (b). Since the maximum quantumness occurs at the same location as the coherence peak, we can say that there is quantum coherence occurring at $S = 0.01$ and $\Delta\epsilon/\omega_0 = 1.5$. Although quantum effects are present at high $\Delta\epsilon$ and S values, there is no coherence at these points.

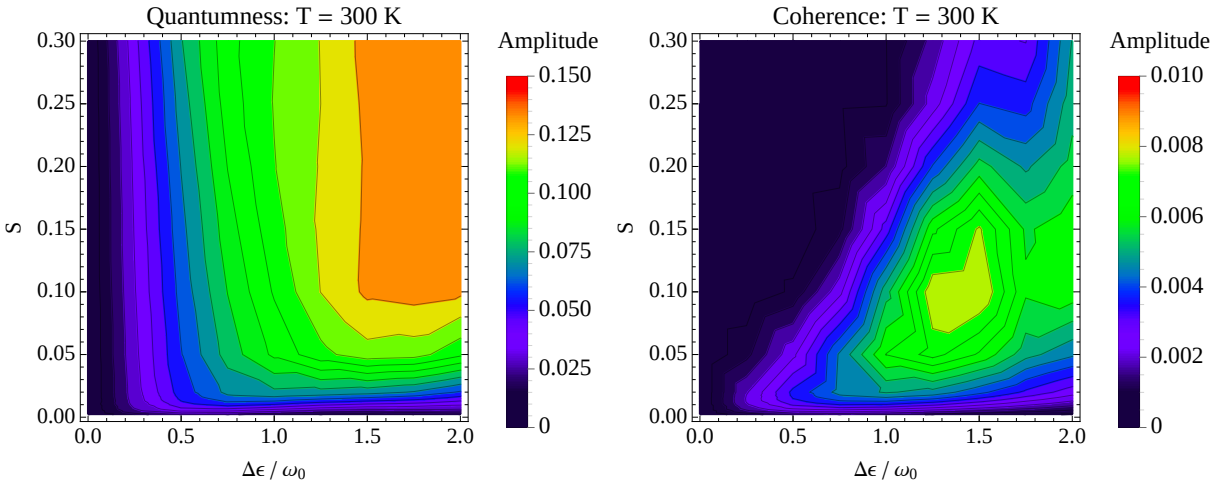

(a) (b)

Figure 6: The contour plots show the quantumness (left) and coherence (right) as the Huang-Rhys factor, S, and energy difference, $\Delta\epsilon/\omega_0$, changes. Both data sets were taken at a temperature of 300 K with an electronic coupling of 100 cm^{-1}. The reorganization energy for each pigment was 15 cm^{-1}.

4.3 Reorganization Energy Difference

Variance in the reorganization energy difference, $\Delta\lambda$, leads to much larger values of quantumness than variance in the Huang-Rhys factor. At 300 K we found a maximum quantumness value of 0.285 occurring at $\Delta\epsilon/\omega_0 = 0$ and $\Delta\lambda$ = -5 fig. 7 (a). The maximum coherence was found to be 0.00465 occurring at $\Delta\epsilon/\omega_0 = 0.75$ and $\Delta\lambda$ = -2 fig. 7 (b). These two peaks do not coincide. However, varying the $\Delta\lambda$ can lead to higher quantumnesses than varying S. There is a minimum at $\Delta\lambda = 0$ and as $\Delta\epsilon/\omega_0$ this minimum does not increase much. Thus, to have significant quantumness and coherence, there needs to be a $\Delta\lambda$ value with a magnitude greater than 2 cm^{-1}.

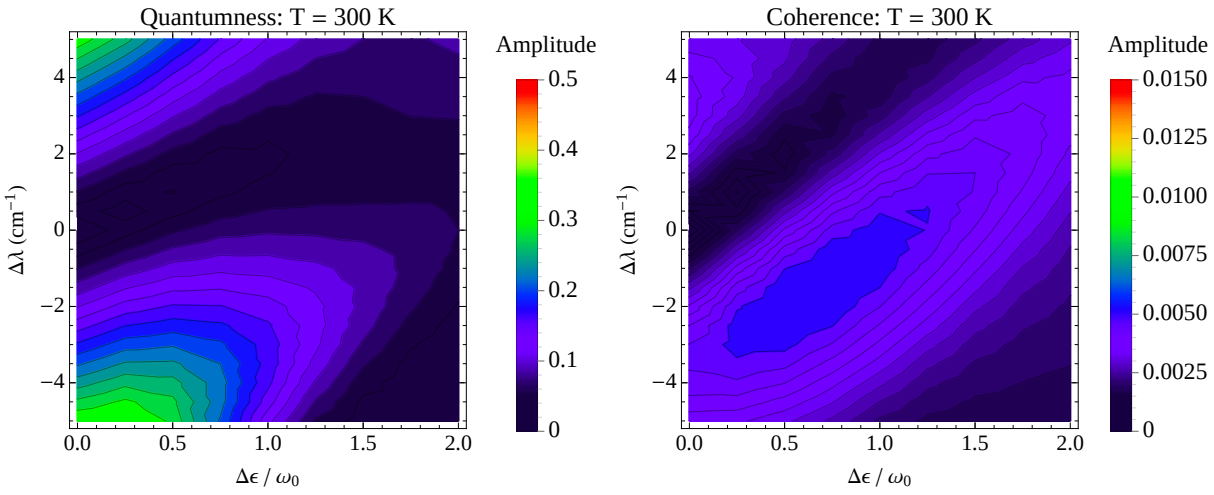

(a) (b)

Figure 7: The contour plots show the quantumness (left) and coherence (right) as the reorganization energy difference, $\Delta\lambda$, and energy difference, $\Delta\epsilon/\omega_0$, changes. Both data sets were taken at a temperature of 300 K with an electronic coupling of 100 cm^{-1}. The base reorganization energy for each pigment was 15 cm^{-1}. The Huang-Rhys factor is set to 0.02.

4.4 BChl Dimer in FMO Complex

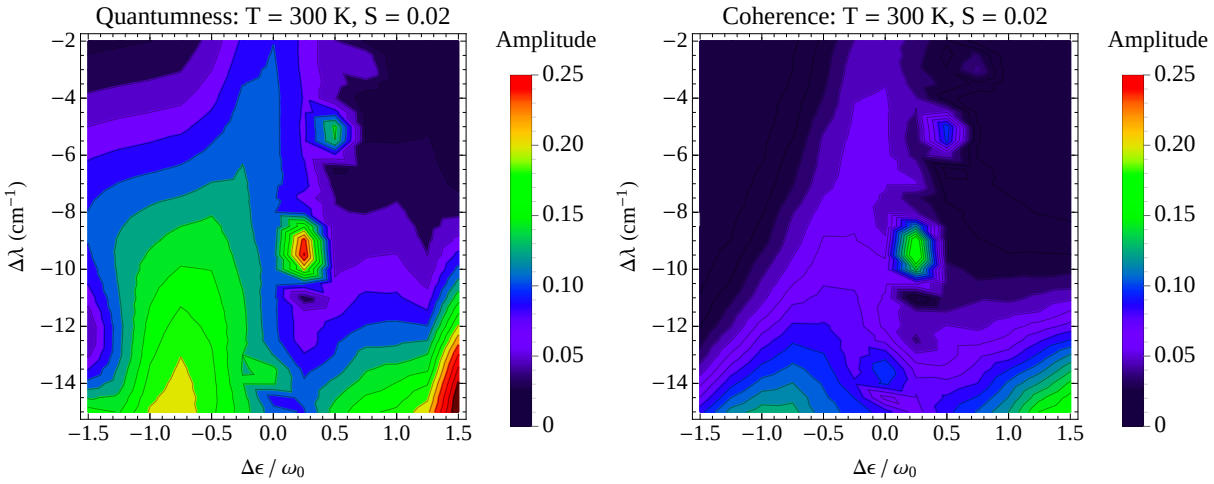

(a) (b)

Figure 8: The contour plots show quantumness (left) and coherence (right) for physiological conditions in the FMO Complex. Electronic coupling and orientation are set to the experimental values for BChl3 and BChl4 as determined by Rivera *et al.* The Huang-Rhys factor is set to 0.02, the base reorganization energy is set to 25 cm^{-1} and the temperature is at 300 K. Both plots are on the same amplitude scale.

There is a lot of overlap between the quantumness and coherence at the physiological conditions of the FMO dimer fig. 8. Plotting the quantumness against the coherence gives a linear trend that can be seen in fig. 9. The linearity means that almost all of the observed coherence is quantum in nature. Furthermore, a very large peak in both quantumness and coherence located at $\Delta\epsilon/\omega_0 = 0.25$ cm^{-1} and $\Delta\lambda = -9.5$ cm^{-1}. The

quantumness at this peak is 0.23 and the coherence at this peak is 0.15. The coherence here is larger than the rest of our data by a factor of 10. Furthermore, there is another peak of lesser magnitude located at $\Delta\epsilon/\omega_0 = 0.5$ cm^{-1} and $\Delta\lambda = -5$ cm^{-1}. At the bottom right hand corner of the plots in fig. 8 there is another maximum emerging. Since the maximum occurs at the boundary of our physiological conditions we will not worry about it.

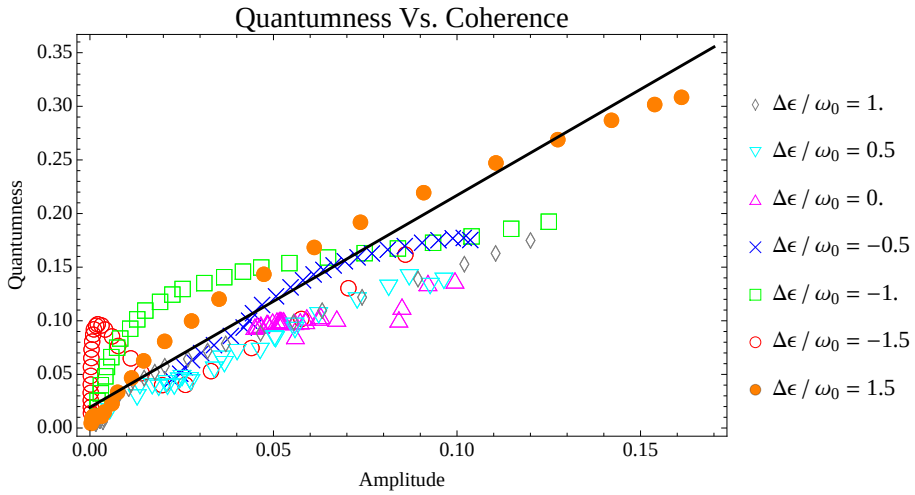

Figure 9: The plot shows the correlation between the quantumness and coherence for the physiological FMO dimer. The data has been fit with a linear model $y = 1.977x + 0.019$. Different colored markers correspond to the energy differences in the legend. Each marker corresponds to a different reorganization energy difference.

Increasing the Huang-Rhys factor does not affect the magnitude of the peaks fig. 10. However, it does change the location. At a Huang-Rhys factor of 0.2, the peak of the quantumness occurs at $\Delta\epsilon/\omega_0 = 0.25$ cm^{-1} and $\Delta\lambda = -8$ cm^{-1} with a maximum of 0.23. The coherence peak occurs at the same location with a maximum of 0.15. These maximum values are unchanged from the results of a Huang-Rhys of 0.02. Since the coherence and quantumness peaks coincide, there is a significant amount of quantum coherence at these peaks. To better understand these peaks we need to look at them in higher $\Delta\lambda$ and $\Delta\epsilon/\omega_0$ resolution.

Zooming in on these peaks (fig. 10 (c) and (d)) shows that there are actually two peaks located close together. These peaks occur at $\Delta\epsilon/\omega_0 = 0.2$ cm^{-1} and $\Delta\lambda = -9.5$ cm^{-1} and at $\Delta\epsilon/\omega_0 = 0.3$ cm^{-1} and $\Delta\lambda = -7$ cm^{-1}. Looking at the peaks at higher resolution does not resolve a higher magnitude. From fig. 8 and fig. 10 we can see that there seems to be regularity to the local maxima and minima. The minimum occurs at $\Delta\lambda = -11$ and $\Delta\epsilon/\omega_0 = 0.25$ in fig. 8 and $\Delta\lambda = -10$ and $\Delta\epsilon/\omega_0 = 0.25$ in fig. **??**. To understand these peaks we must look at the raw coherence data fig. 11.

4.5 Discussion

Looking at the coherence for the two peaks fig. 11 (a) and (b), the minimum fig. 11 (c), and the transition between the peak and minimum fig. 11 (d), we find that every data point occurs at roughly the same amplitude. This indicates that the frequency the coherence is

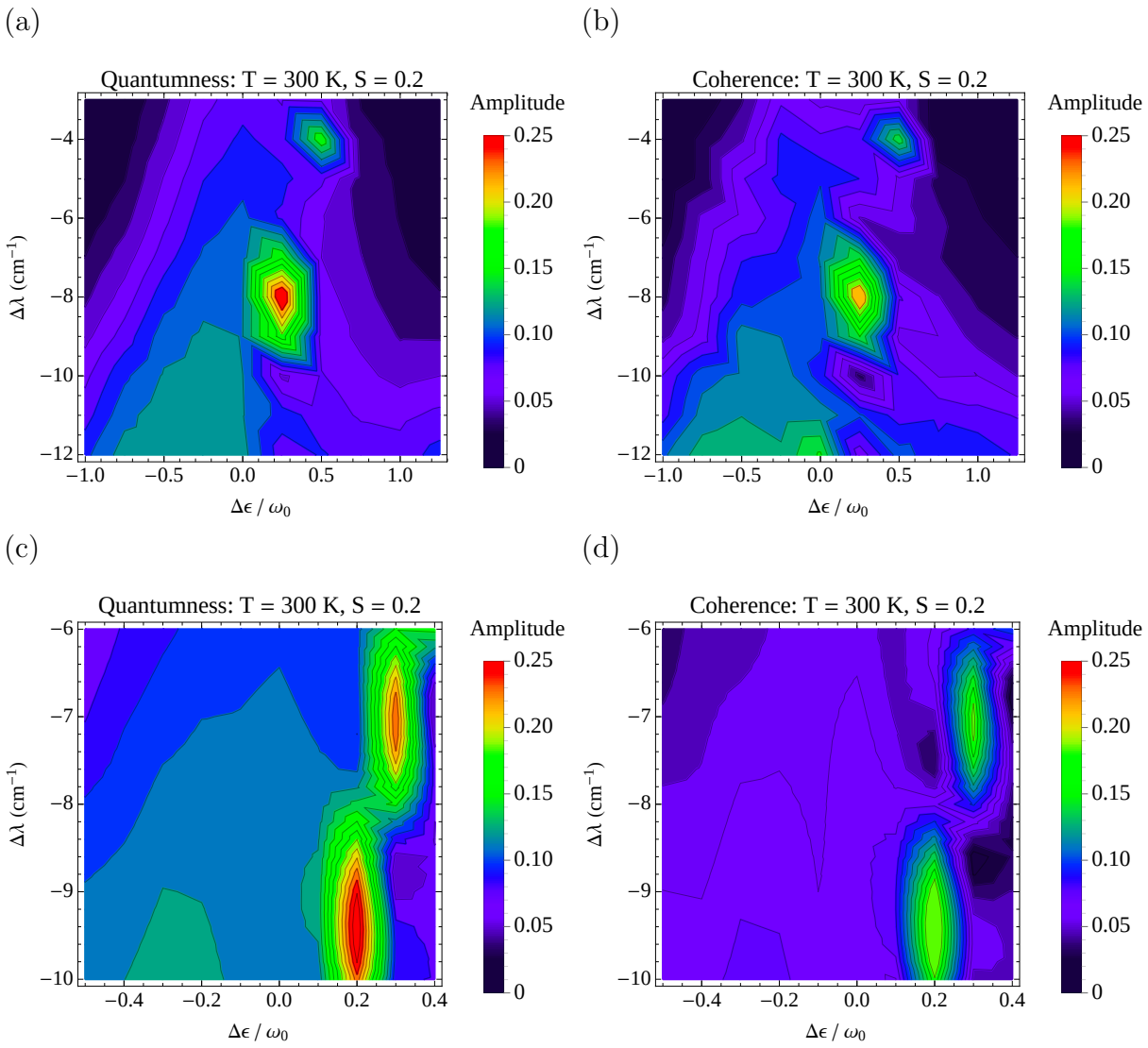

Figure 10: The contour plots show quantumness (left) and coherence (right) for physiological conditions in the FMO Complex. The condition are the same as fig. 8 except for the Huang-Rhys factor which is set to 0.2. Plots (c) and (d) are higher resolution plots of (a) and (b) respectively. All plots are on the same amplitude scale.

oscillating at corresponds to the length of the time slice (Δt) of the simulation. Fitting the real part of the coherence with a cosine function, we find that for each of plots, the frequency of oscillation is about $3.7\omega_0$. This frequency corresponds to a period of 50 fs which is $2\Delta t$. Thus, for every time slice of the simulation, we will be sampling the same part of the coherence. For example, the sample may be taken from the peaks every time or from the origin every time. Having a sample rate that corresponds to the period of coherence has a few effects on our data.

As the phase of the coherence changes, the simulation will cycle through sampling from the peak fig. 11 (a) to the origin fig. 11 (d). When we repeatedly sample from a peak, the simulation will show that there is a lot of coherence, furthermore, when we repeatedly sample from the origin, the coherence will seem nonexistent. However, the coherence can be just as strong in both of these cases, just hidden by the poor sampling

(a)

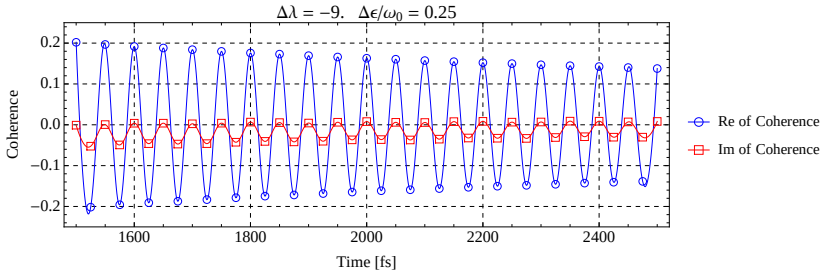

(b)

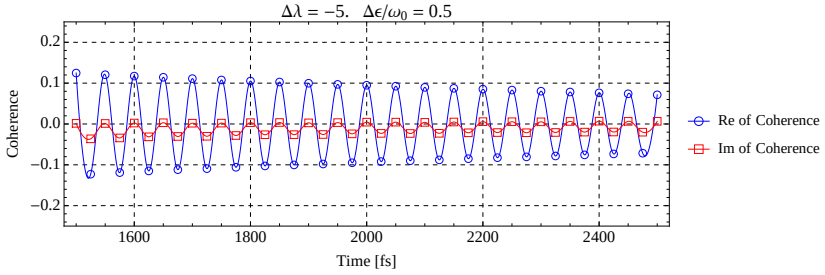

(c)

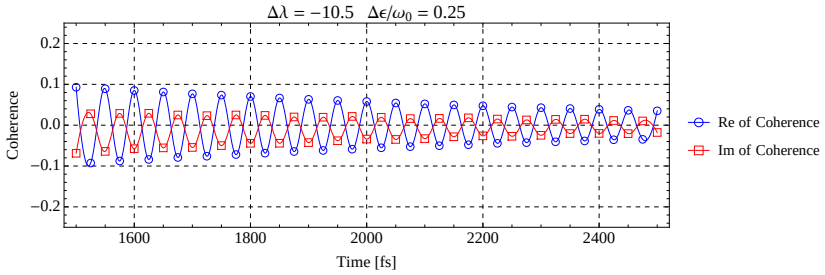

(d)

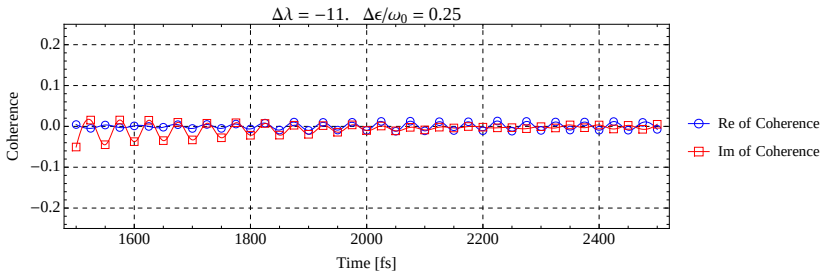

Figure 11: The plots show the real and imaginary parts of the coherence for the last 1000 fs of the data shown in fig. 8. Plot (a) corresponds to the largest peak, plot (b) corresponds to the secondary peak, plot (c) corresponds to the transition into the minimum, and plot (d) corresponds to the local minimum.

of the simulation. The maxima and minima that occurred regularly in the FMO data all have coherence frequencies $3.7\omega_0$. The phase of the coherence must be changing with the reorganization energy. Thus causing the coherence to come in and out of phase with the time slices giving the appearance of regular coherent peaks. Furthermore, if there are maximal values in the off diagonals of the density matrix every time the quantumness is calculated, then the quantumness will be larger. Likewise, if there are minimal values in the off diagonals the quantumness will be small. This is why the quantum maxima and minima coincide with coherence maxima and minima.

Since the coherence was analyzed by looking at the rms of the real part, data where all of the samples are taken from the same amplitude will be skewed. If all of the data points are at the peak of the coherence oscillation, then the rms will give the value of the peak. If the samples are taken equally from all parts of the coherence, then the rms will give a value closer to $a/\sqrt{2}$ where a is the amplitude of the oscillation. The maximal rms value of coherence for the FMO was found to be 0.15, this is where the samples were taken from the peak of the coherence at each time slice. If the samples were taken randomly from the coherence, then the rms value would be closer to $0.15/\sqrt{2} \approx 0.1$. Thus, There may be coherences just as strong as the peak at locations where the coherence was equal to 0.1, such as the blue sections of fig. 8 (b).

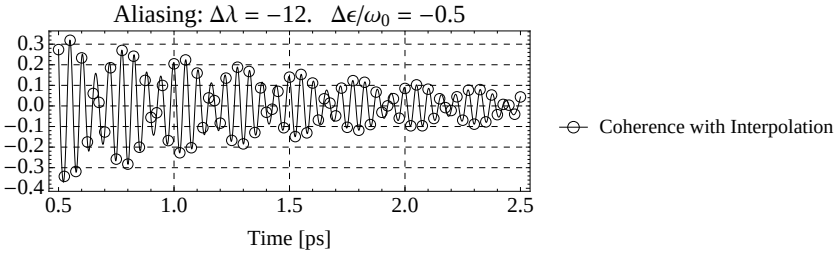

Figure 12: The plot shows the real part of the coherence aliasing. The data was taken from the physiological FMO dimer with Huang-Rhys factor of 0.02. The energy difference and reorganization energy difference are labeled above the figure. If you look at the data points (the circles), you can see two slowly oscillating anti-correlated sine waves. These low frequency oscillations are a direct result of aliasing.

Because the simulation sample rate is on the same order as the coherence period, aliasing will become an important factor. Aliasing is a distortion in the signal due to the sample rate being slower than the period of oscillation fig. 12. When a signal aliases, its amplitude will appear to have a secondary low frequency oscillation in addition to the normal oscillations of the wave. This is because when each a sample is taken, it is at a phase slightly behind the previous sample. Over time, the phase will get so far behind that samples are taken at the peak again. The actual frequency of the coherence in fig. 12 is $\approx 4.07\omega_0$ which corresponds to a period of 45.5 fs. The time slice Δt of the simulation is 25 fs. Thus for every two samples, there will be a lag of 5 fs. After 10 samples, the simulation will be sampling from the peak again.

5 Conclusion

We found that increasing the Huang-Rhys factor to 0.1 increases the long-term quantumness. Increasing the Huang-Rhys factor further has little effect on the quantumness and decreases the coherence. The long-term coherence peaks at a Huang-Rhys factor of 0.1. We found greater changes in quantumness and coherence by varying the site energy difference and reorganization energy difference. Understanding how the long-term quantum coherence behaves in different conditions is essential in designing devices that exhibit long-term coherence. Furthermore, inclusion of quantized normal modes is needed to create these long-lived oscillations. In the physiological BChl dimer in the FMO, we found a maximum quantumness of 0.23 and a maximum coherence of 0.15. The coherence was a magnitude of 10 larger than any of the data sets we took. These maximums coincide suggesting that long-lived quantum coherences may exist in the FMO Complex at physiological conditions. However, the temporal resolution of our simulation was not high enough allowing for aliasing in our coherence data. Until we improve the time resolution of our simulation, we cannot conclude if significant quantum coherences occur in the FMO at physiological conditions.

Bibliography

[1] Niklas Christensson, Harald F. Kauffmann, Tonu Pullerits, and Tomás Mančal. Origin of long-lived coherences in light-harvesting complexes. *J. Phys. Chem. B*, 116:7449–7454, 2012.

[2] Gitt Panitchayangkoon, Dugan Hayes, Kelly A. Fransted, J. R. Caram, E. Harel, R. E. Wen, J. Blankenship, and G. S. Engel. Long-lived quantum coherence in photosynthetic complexes at physiological temperature. *Proc. Natl. Acad. Sci.*, 107:12766–12770, 2010.

[3] Edward J. O'Reilly and Alexandra Olaya-Castro. Non-classicality of the molecular vibrations assisting exciton energy transfer at room temperature. *Nature Communications*, January 2014.

[4] P. Nalbach, J. Eckel, and M. Thorwart. Quantum coherent biomolecular energy transfer with spatially correlated fluctuations. *New. J. Phys.*, 12:065043/1–065043/18, 2010.

[5] Maximillian Schlosshauer. *Decoherence and the Quantum-to-Classical Transition.* Springer-Verlag Berlin Heidelberg, 2007.

[6] W. H. Zurek. Decoherence and the transition from quantum to classical. *Phys. Today*, 44:36–44, 1991.

[7] Olivier Giraud, Peter Braun, and Daniel Braun. Quantifying quantumness and the quest for queens of quantum. *New. J. Phys.*, 12(063005):063005/1 – 063005/22, June 2010.

[8] T. Renger, A. Klinger, F. Steinecker, M. Schmidt am Busch, J. Numata, and F. Müh. Normal mode analysis of the spectral density of the fenna-matthews-olson light-harvesting protein: How the protein dissipates the excess energy of excitons. *J. Phys. Chem. B*, 116:14565–14580, 2012.

[9] Jordan M. Womick and Andrew M. Moran. Vibronic enhancement of exciton sizes and energy transport in photosynthetic complexes. *The Journal of Physical Chemistry B*, 115:1347–1356, January 2011.

[10] John Whitmarsh, Govindjee, ed. GS Singhal, and ed. G Renger. The photosynthetic process, 1995.

[11] Robert E. Blankenship. *Molecular Mechanisms of Photosynthesis.* Blackwell Science, 2002.

[12] Volkhard May and Oliver Kühn. *Charge and Energy Transfer Dynamics in Molecular Systems.* Wiley-VCH, Weinheim, Germany, third, revised and enlarged edition, 2011.

[13] Julia Adolphs and Thomas Renger. How proteins trigger excitation energy transfer in the fmo complex of green sulfur bacteria. *Biophysical Journal*, 91:2778–2797, October 2006.

[14] Sergey Polyutov, Oliver Kühn, and Tonu Pullerits. Exciton-vibrational coupling in molecular aggregates: Electronic versus vibronic dimer. *Chemical Physics*, 394:21–28, December 2012.

[15] J. J. Sakurai. *Modern Quantum Mechanics*. Addison-Wesley, Reading, Massachusetts, 1994.

[16] N. Makri and D. E. Makarov. Tensor porpagator for iterative quantum time evolution of reduced density matrices. i. theory. *J. Chem. Phys.*, 102:4600–4610, 1995.

[17] N. Makri and D. E. Makarov. Tensor porpagator for iterative quantum time evolution of reduced density matrices. ii. numerical methodology. *J. Chem. Phys.*, 102:4611–4618, 1995.

[18] P. Nalbach, A. Ishizaki, G. R. Fleming, and M. Thorwart. Iterative path-integral algorithm versus cumulant time-nonlocal master equation approach for dissipative biomolecular exciton transport. *New. J. Phys.*, 13:063040/1–063040/13, 2011.

[19] R. Feynman and F. L. Vernon. The theory of a general quantum system interacting with a linear dissipative system. *Ann. Phys. N.Y.*, 24:118–173, 1963.

[20] Margus RR̈atsep Zheng-Li Cai, Jeffrey R. Reimers, and Arvi Freiberg. Demonstration and interpretation of significant asymmetry in the low-resolution and high-resolution qy fluorescence and absorption spectra of bacteriochlorophyll a. *The Journal of Chemical Physics*, 134, January 2011.

[21] E. Rivera, D. Montemayor, M. Masia, and D. F. Coker. Influence of site-dependent pigment-protein interactions on excitation energy transfer in photosynthetic light harvesting. *J. Phys. Chem. B*, 117(18):5510–5521, 2013.